Atmospheric
Chemistry
and Physics

Supplement of

CALIPSO (IIR–CALIOP) retrievals of cirrus cloud ice-particle concentrations

David L. Mitchell et al.

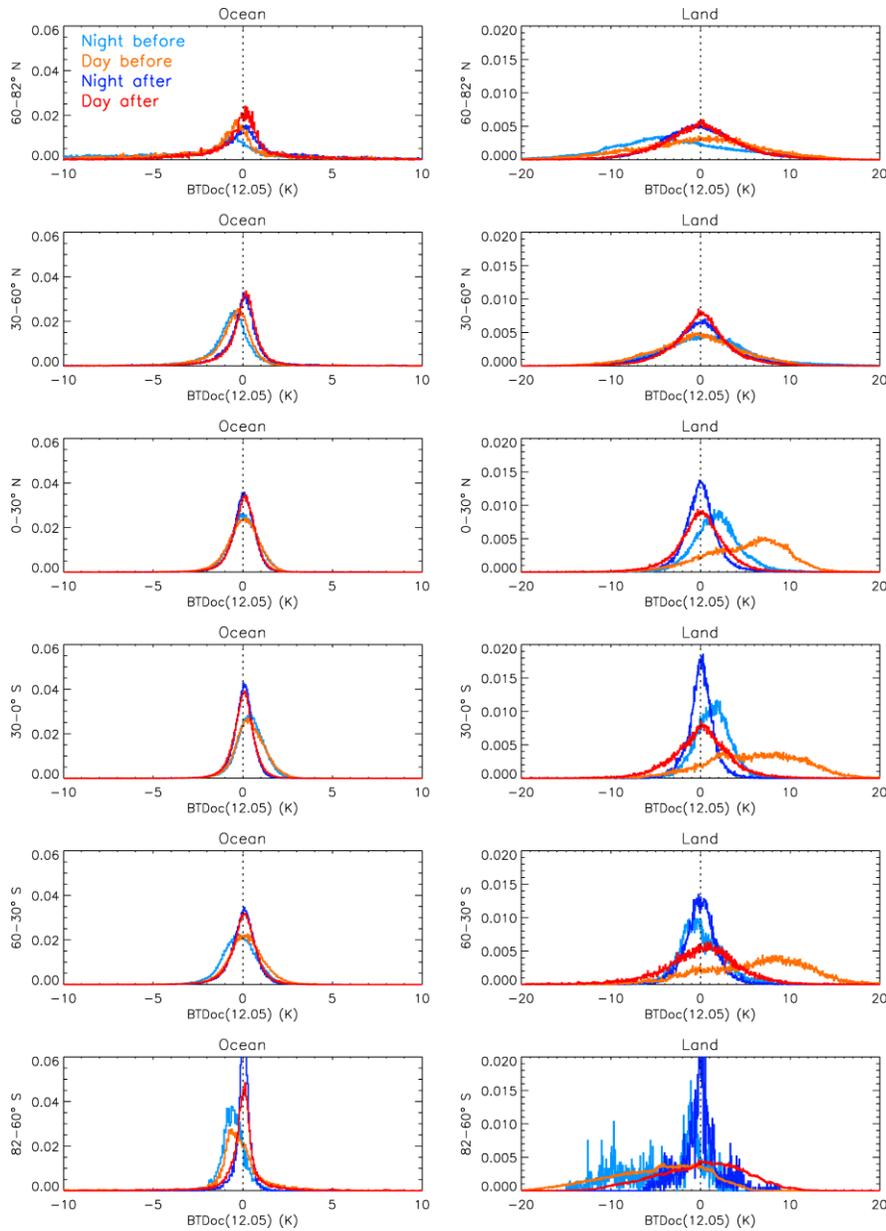*Correspondence to:* David Mitchell (david.mitchell@dri.edu)

Figure S1a: Probability density functions of the differences between clear sky observations and computations of brightness temperature (BTDoc) at 12.05 μm, before (night: light blue; day: orange) and after (night: navy blue; day: red) correction for six latitude bands over ocean (left) and over land (right) in January 2008. Note the different scales over ocean and over land.
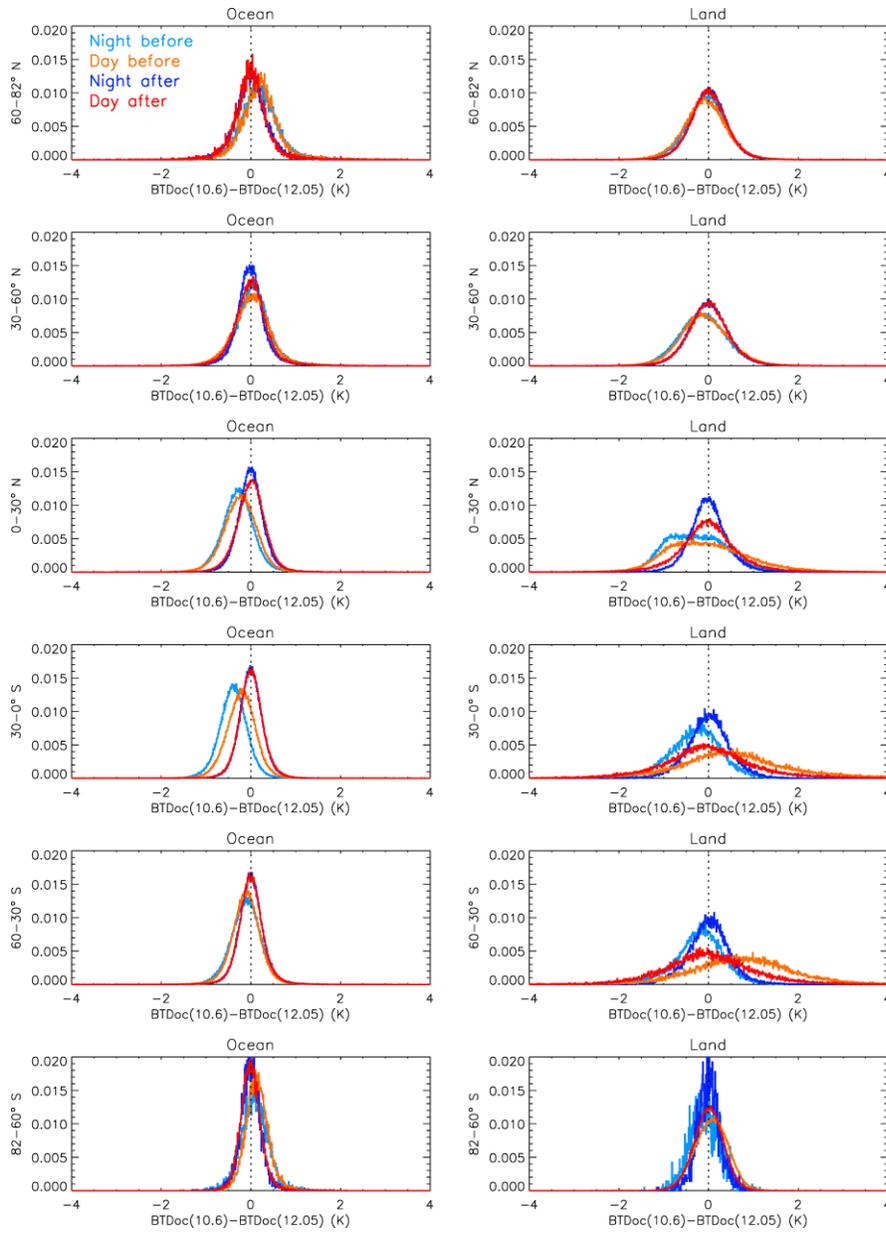
Figure S1b: Same as Fig. S1a, but for the inter-channel difference between observations and computations, BTDoc(10.6 μm)-BTDoc(12.05 μm).

Impact of the smallest size bin in PSD measurements

Jensen et al. (2013a) argues that the PSD first bin $N(D)_1$ as measured by the 2D-S probe is anomalously high since it tends to be considerably higher than the adjacent size-bins [$N(D)_2$ for example] and that these small ice crystals should rapidly grow or sublimate to larger or smaller sizes (> 15 μm or < 5 μm) due to the relative humidity with respect to ice, RH_i, being significantly different than ice saturation ($RH_i = 100$ %). Therefore, $N(D)_1 > N(D)_2$ would imply frequent ice nucleation events to sustain these higher $N(D)_1$ values, which appears unlikely. This argument provided an additional incentive to formulate this retrieval assuming $N(D)_1 = 0$.

However, there are also physical reasons that argue in favor of assuming that $N(D)_1$ is a valid measurement. For example, if strong competition for water vapor due to a relatively high small ice crystal concentration (e.g. due to a homogeneous ice nucleation event) rapidly reduces the RH_i to ~ 100%, then this relatively high concentration may last for time periods comparable to the lifetime of the cirrus cloud. High ice crystal concentrations (~ 300 to 10,000 L^{-1}) associated with RH_i ~ 100% were documented by aircraft measurements in the tropical tropopause layer (TTL), existing in layers ranging from meters to 0.4 km in depth (Jensen et al., 2013b). These layers were embedded within a deeper cirrus cloud having N typically less than 20 L^{-1} (where RH_i was higher). Evidence that RH_i near 100% is common in cirrus clouds is shown in Figs. 6 and 7 of Krämer et al. (2009), where for the relationships most representative of cirrus clouds, the relaxation time τ for RH_i to develop a quasi-steady state (i.e. dynamical equilibrium denoted RH_{qsi}) is on the order of 5-10 minutes. RH_{qsi} is where $d(RH_i)/dt \approx 0$, where the rate of vapor uptake by ice approximately balances the rate of supersaturation development. Between the time of initial in-cloud supersaturation (corresponding to cloud formation) and τ, the cloud updraft w tends to be higher than the w occurring after RH_{qsi} is attained. Since cirrus cloud lifetimes tend to be considerably longer than 5-10 minutes, w is relatively low with RH_i ~ 100 % for time $t > \tau$. This may explain the relatively high frequencies of occurrence of RH_i near 100 % in Fig. 7 of Krämer et al. (2009). It can also be argued that cirrus clouds are formed by atmospheric wave activity, and that RH_i near 100 % results from averaging transient wave-induced fluctuations of RH_i. However, Fig. 1 in Krämer et al. (2009) shows water vapor concentrations being fairly constant with time over periods of 30 to 50 minutes, while also showing evidence of wave-induced fluctuations in RH_i during another period.

Comparisons between the Fast Cloud Droplet Probe (FCDP) and the 2D-S probe during ATTREX when sampling tropical tropopause layer (TTL) cirrus clouds (Woods et al., 2018, Fig. 3) show that the smallest 2D-S size bin often, but not always, measured a lower $N(D)_1$ than did the FCDP. These clouds were not in close proximity to deep convection and were sustained over relatively long periods.
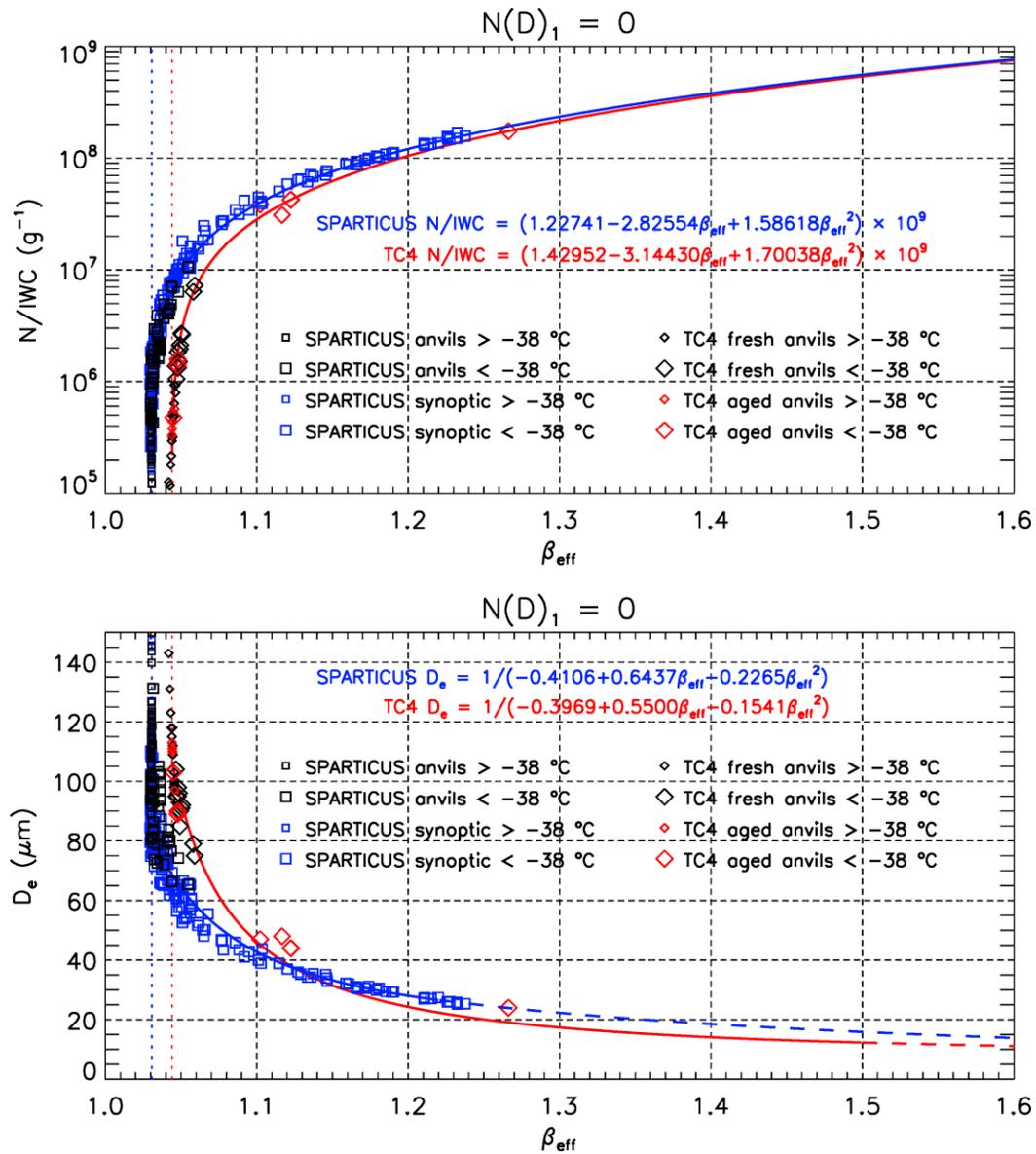
Figure S2: Same as Fig. 2 (top) and Fig. 3 (bottom) in the main paper, but in this case the first size-bin of the PSD is not included (i.e. $N(D)_1 = 0$). The dashed lines in the lower panel are where the curve-fit equations giving $1/D_e$ in μm^{-1} are extrapolated (see Table 1 in main paper).
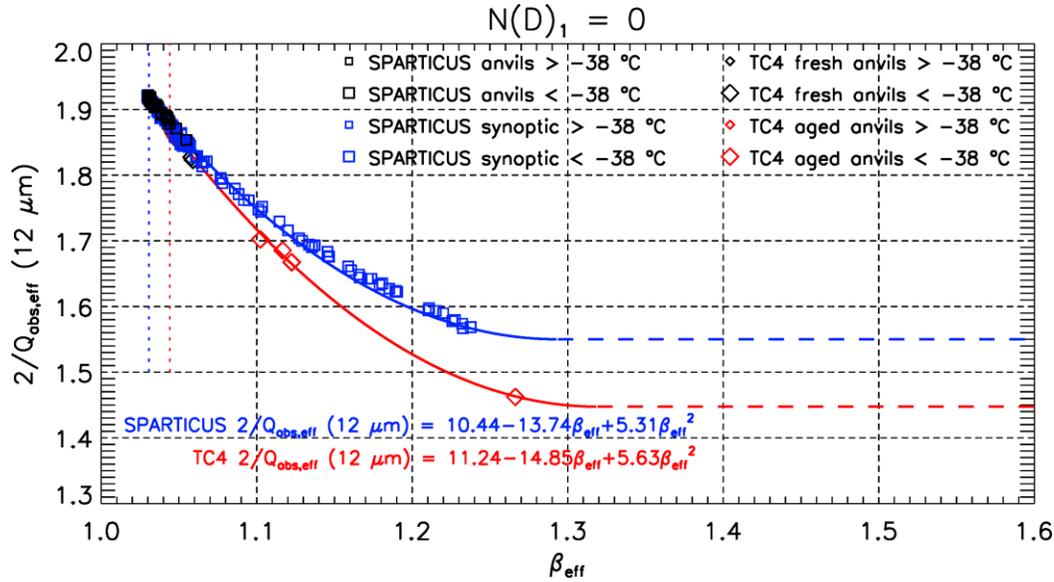
Figure S3: Same as Fig. 4 in the main paper, but in this case the first size-bin of the PSD is not included (i.e. $N(D)_1 = 0$).. **The dashed lines are where the curve-fit equations are extrapolated (see Table 1 in main paper).**

The figure contains:

$N(D)_1 = 0$

Legend:
- SPARTICUS anvils > −38 °C
- SPARTICUS anvils < −38 °C
- SPARTICUS synoptic > −38 °C
- SPARTICUS synoptic < −38 °C
- TC4 fresh anvils > −38 °C
- TC4 fresh anvils < −38 °C
- TC4 aged anvils > −38 °C
- TC4 aged anvils < −38 °C

$$\text{SPARTICUS } 2/Q_{obs,eff} \ (12 \ \mu m) = 10.44 - 13.74\beta_{eff} + 5.31\beta_{eff}^2$$
$$\text{TC4 } 2/Q_{obs,eff} \ (12 \ \mu m) = 11.24 - 14.85\beta_{eff} + 5.63\beta_{eff}^2$$

y-axis: $2/Q_{obs,eff}$ $(12 \ \mu m)$
x-axis: β_{eff}

Relationship between β_{eff}, α_{ext}, IWC, and N

As seen from Eq. (6), (7) and (8), β_{eff} and α_{ext} are the two key parameters retrieved from the CALIPSO IIR to derive N/IWC, IWC, and finally N. The interrelationship between β_{eff}, α_{ext}, IWC, and N is illustrated in Fig. S4 (top row) for the SPARTICUS relationships using the unmodified $N(D)_1$ assumption, which also shows the range encountered for these properties in the selected cloud population. The red dashed lines are where N = 100 L^{-1}, 500 L^{-1} and 1000 L^{-1}. The pink dashed lines are where IWC = 0.5 mg m^{-3}, 5 mg m^{-3}, or 30 mg m^{-3}. The horizontal red dotted lines for $\beta_{eff} < 1.031$ (or $D_e > 83$ μm) indicate where the retrieval is not sensitive to N/IWC. For $\beta_{eff} < 1.031$, N/IWC is set to its limiting (minimum) value so that N is a priori overestimated in these conditions, but typically smaller than 100 L^{-1}. For $\beta_{eff} < 1.031$, D_e is set to 83 μm, as denoted by the horizontal pink lines, and IWC is a priori underestimated for these conditions. For our data selection, α_{ext} is mostly between 0.05 km^{-1} and 5 km^{-1}. Large values of N (> 500 L^{-1}) result from larger values of β_{eff} (yielding smaller D_e and much larger N/IWC) and sufficiently large values of α_{ext} so that IWC is sufficiently large for these small values of D_e. Low values of N (< 100 L^{-1}) can be retrieved for small values of β_{eff}, yet larger than the low limit of 1.031, only if α_{ext} is sufficiently small.

This same analysis was repeated in Fig. S5, except the sample selection criteria for minimum OD was changed from 0.3 to 0.1. This increased the sample population considerably. The larger dispersion in β_{eff} and in particular the larger portion of samples with β_{eff} much smaller than 1 (Fig. S5, top row) are due to large uncertainties at OD between 0.1 and 0.3, which also explain the larger portion of samples with $\Delta N/N > 1$ (Fig. S5, bottom row). More samples now correspond to lower values of α_{ext} (down to 0.016 km^{-1}), IWC, and N.
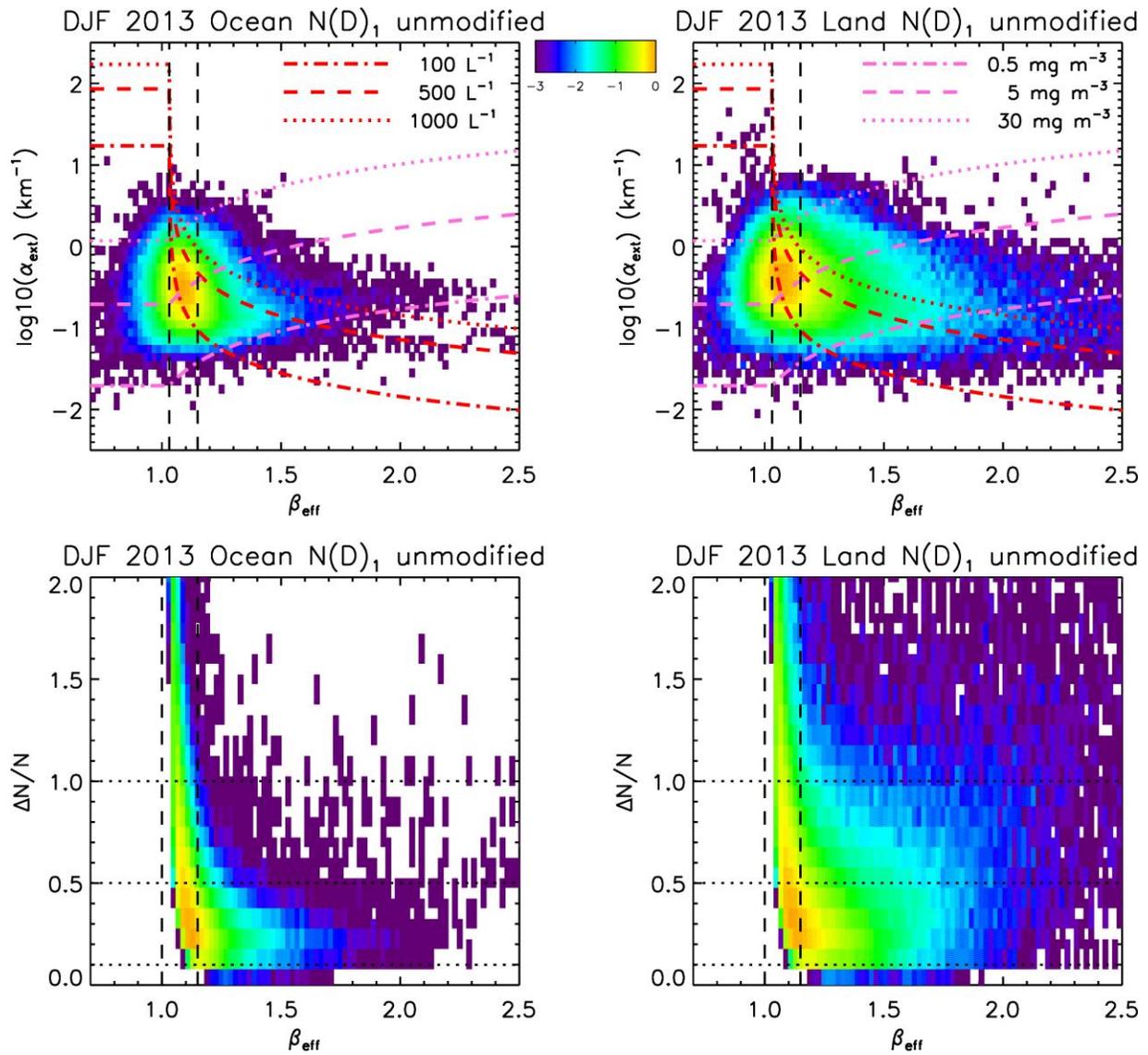
Figure S4: **Top: The interrelationship between β_{eff} (X-axis), layer extinction coefficient α_{ext} (km^{-1}) (Y-axis, log10 scale), ice water content IWC, and ice particle number concentration N for the SPARTICUS N(D)$_1$ unmodified assumption. The red dashed lines are where N is equal to 100, 500, or 1000 L^{-1}. The pink dashed lines are where IWC is equal to 0.5, 5, or 30 mg m^{-3}. Bottom: 2D-distribution of β_{eff} (X-axis) and relative uncertainty estimate $\Delta N/N$. The color bar gives the decimal logarithm of number of samples normalized to the maximum value. Relative uncertainty tends to be considerably smaller at larger β_{eff} values. Left: ocean; right: land; all latitudes; based on December 2013, January and February 2014.**
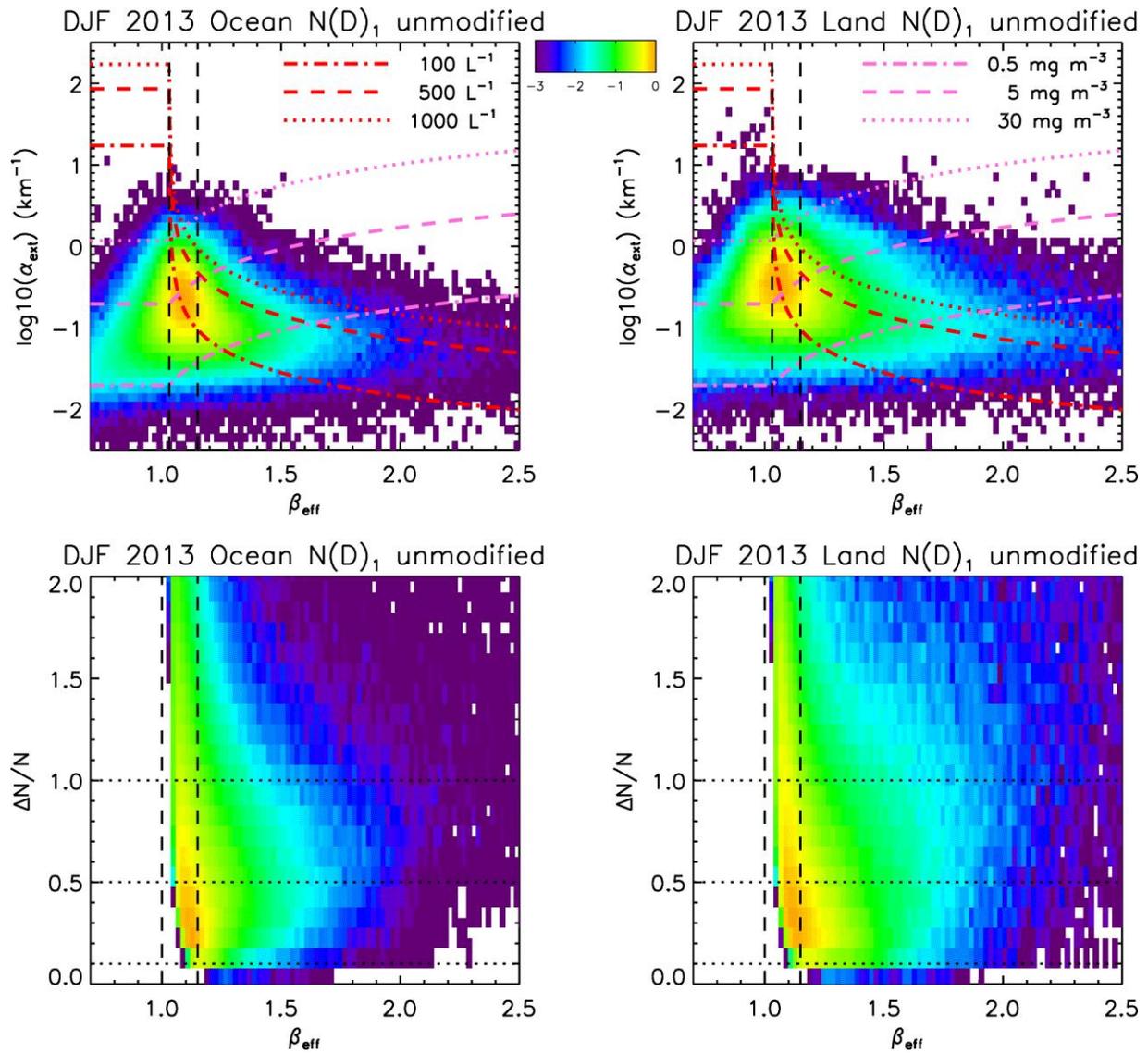
Figure S5: Same as Fig. S4 but the sample selection criteria was changed to accept samples having OD > 0.1 approximately. Note the larger portion of samples having ΔN/N > 1.

Comparison of N/IWC with the Krämer cirrus dataset

Although the cirrus cloud measurements in Krämer et al. (2009) occurred over both land and ocean, no distinction was made in this regard. But since CALIPSO IIR β_{eff} uncertainties are greater over land, Fig. S6 separates in situ and satellite retrievals of N/IWC and β_{eff} over ocean (top) and land (bottom). CALIPSO values are averaged over all seasons for 2013 and over the latitude range roughly corresponding to the field measurements (25° S to 70° N). Temperature intervals are 4 °C.

Shown in the left panels is N/IWC vs. T_c. The N/IWC curve fits describing the in situ measurements of Krämer et al. (2009) are shown by the grey curves, and correspond to the maximum, minimum and middle (i.e. mid-point) value of a cloud property as a function of temperature. They are compared with corresponding retrieved median values, based on our four formulations: SPARTICUS unmodified $N(D)_1$ (solid navy blue), SPARTICUS $N(D)_1 = 0$ (solid light blue), TC4 unmodified $N(D)_1$ (solid red), and TC4 $N(D)_1 = 0$ (solid orange), all derived from IIR β_{eff} shown in the right panels (black curves). The dashed curves give the 25th and 75th percentile retrieval values. Using our four formulations, in situ N/IWC is converted into four in situ β_{eff} plotted in the right panels for comparison with IIR β_{eff} in black. Comparing both N/IWC and β_{eff} allows visualizing the non-linear relationship between N/IWC and β_{eff}.

Note that the Krämer et al. (2009) data used in Fig. S6 contain several non-zero bins between 5 and 15 microns (i.e. the 1st size-bin of the 2DS probe). Thus, the in situ PSD do not conform with the $N(D)_1 = 0$ assumption. However, as shown in Fig. S6 (left panels), the retrieved N/IWC is weakly sensitive to the $N(D)_1$ assumption. Given the above ambiguities and uncertainties, the agreement between the median retrieved and in situ N/IWC is noticeable, especially for both SPARTICUS relationships over land. Both CALIPSO IIR β_{eff} and in situ β_{eff} are smaller than about 1.25 for temperatures greater than 203 K (-70 °C), in agreement with CALIPSO IIR β_{eff} retrieved during SPARTICUS (Fig. 6a in main paper) and during TC4 (Fig. 6b in main paper).
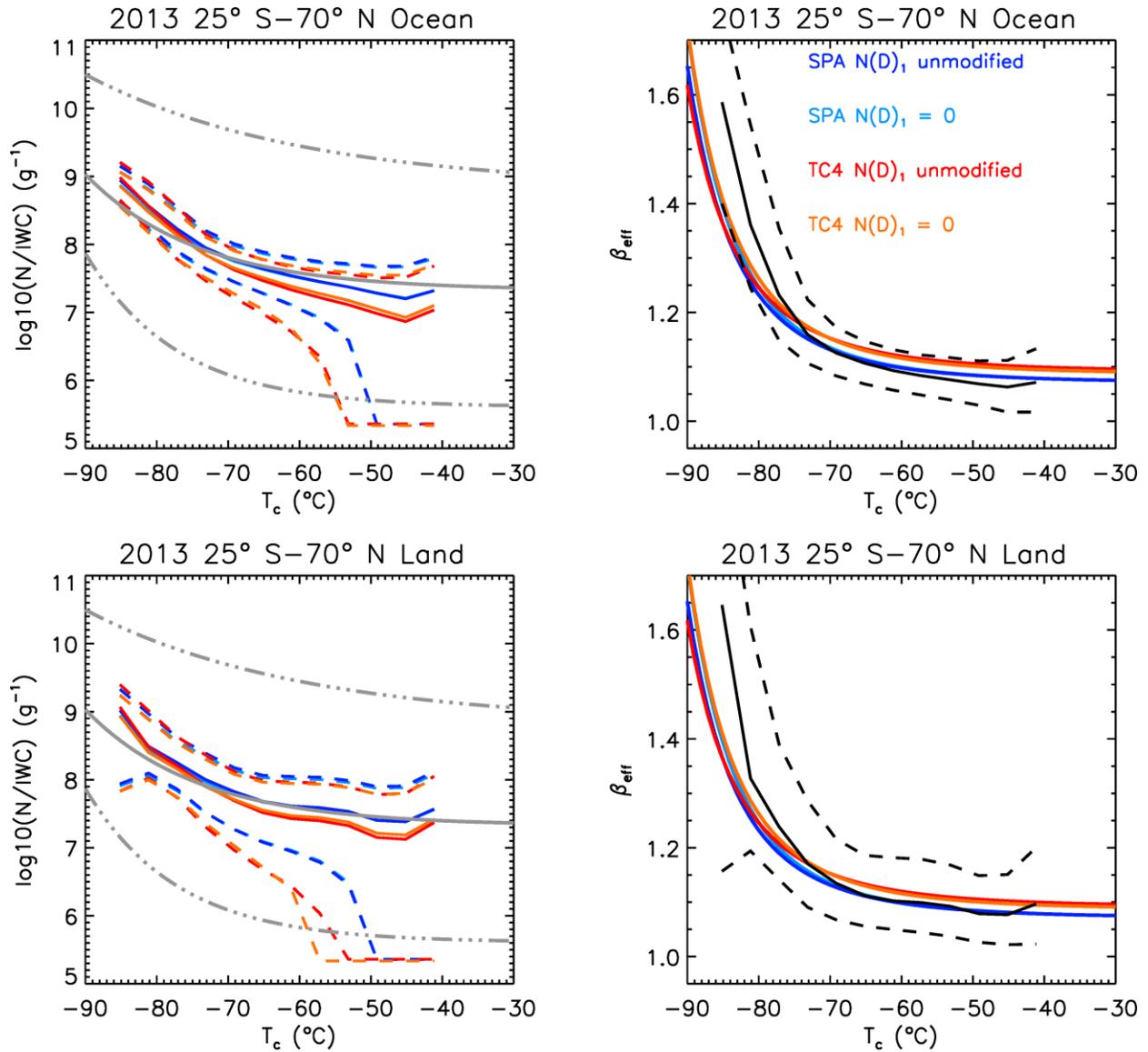
Fig. S6. Left: Comparisons of the median CALIPSO IIR N/IWC (g^{-1}) for the four formulations (colored) with in situ measurements from Krämer et al. (2009) shown by the grey curves; top and bottom being minimum and maximum values and middle grey solid curve being the middle value. Colored solid curves are median values while dashed curves indicate the 25th and 75th percentile values. Right: Comparisons of CALIPSO IIR β_{eff} shown by the black curves (solid curve gives the median value while dashed curves indicate the 25th and 75th percentile values) with the four (colored) in situ β_{eff} inferred from in situ N/IWC (from Krämer et al. (2009)) using the four formulations. Corresponding minimum and maximum values are not shown. The navy and light blue curves correspond to the SPARTICUS formulations for the unmodified N(D)$_1$ assumption and the N(D)$_1$ = 0 assumption, respectively. The red and orange curves are using the TC4 formulations for the N(D)$_1$ unmodified and N(D)$_1$ = 0 assumptions, respectively. The CALIPSO IIR retrievals are from 2013 and are for the approximate latitude range (25° S to 70° N) of the in situ data, over oceans (top) and over land (bottom).
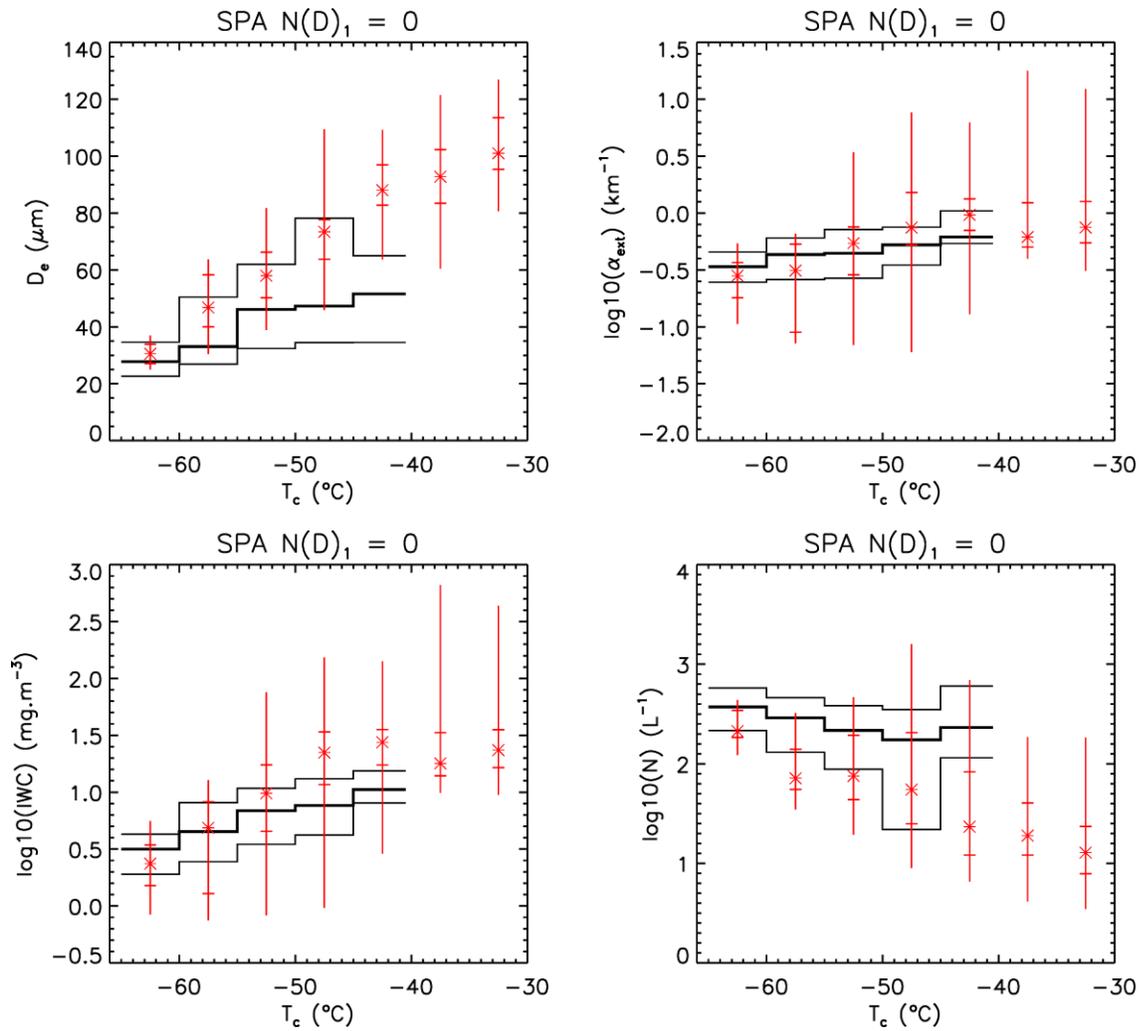
Figure S7. Same as Fig. 7a in the main paper (comparing CALIPSO retrievals with SPARTICUS data), except using the N(D)$_1$ = 0 assumption.
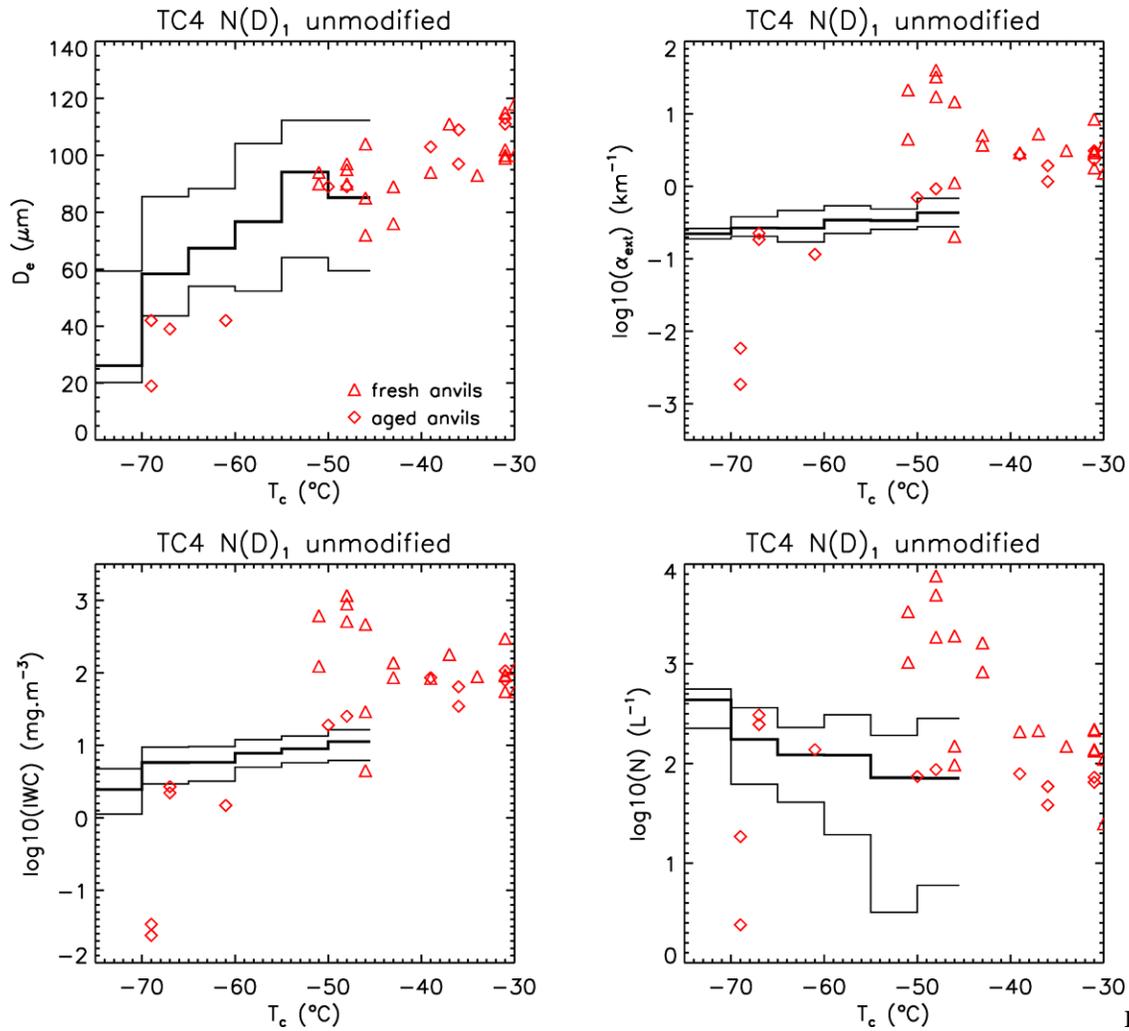
Figure S8. Same as Fig. 7b in the main paper (comparing CALIPSO retrievals with TC4 data), except using the N(D)₁ unmodified assumption.
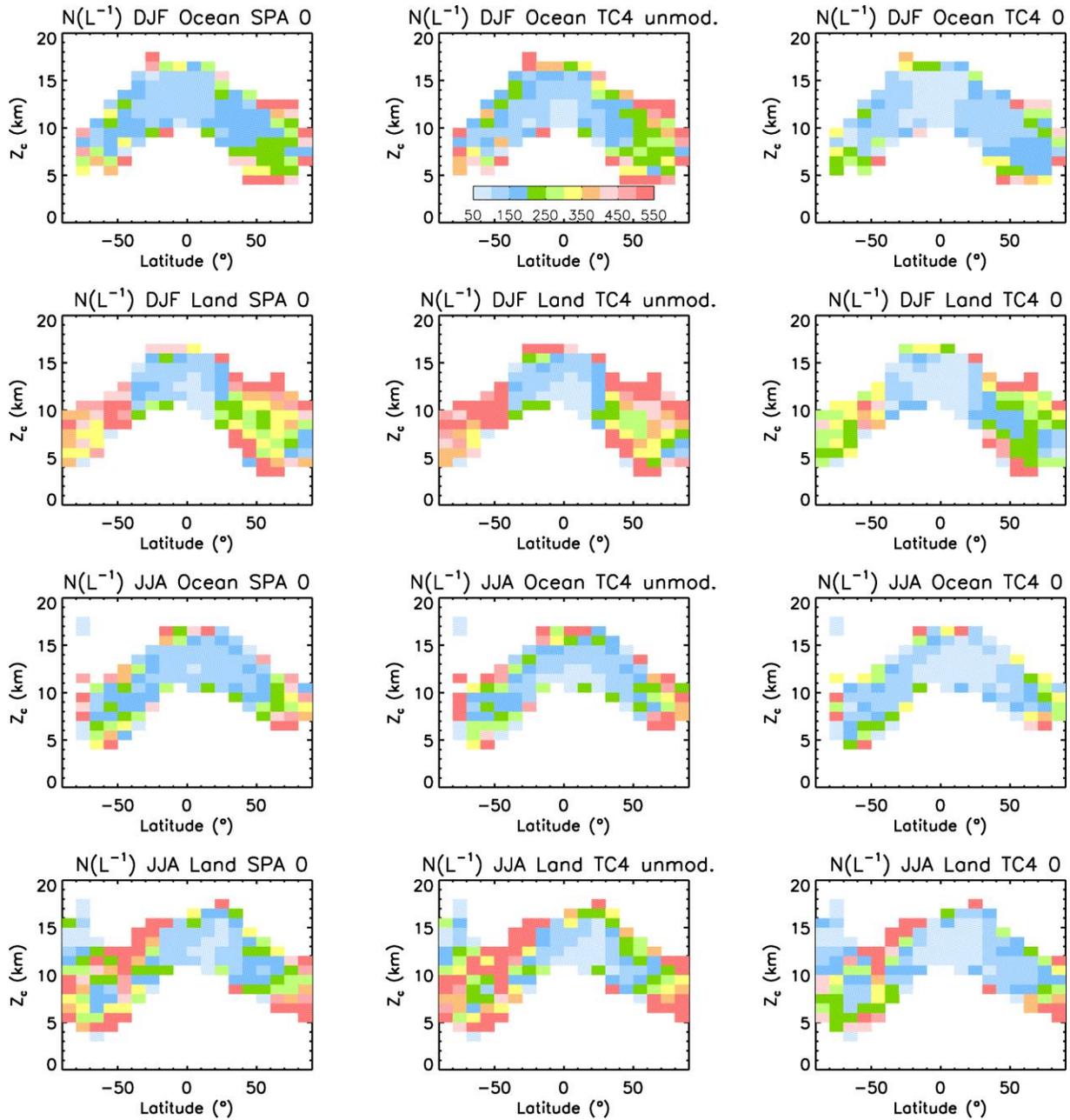
Figure S9: Median ice particle number concentration N (L^{-1}) vs. latitude and representative cloud altitude, Z$_c$, during 2008 and 2013 using three formulations: SPARTICUS N(D)$_1$ = 0 (left), TC4 N(D)$_1$ unmodified (center), and TC4 N(D)$_1$ = 0 (right). Panels from top to bottom are for DJF over oceans, DJF over land, JJA over oceans, and JJA over land.
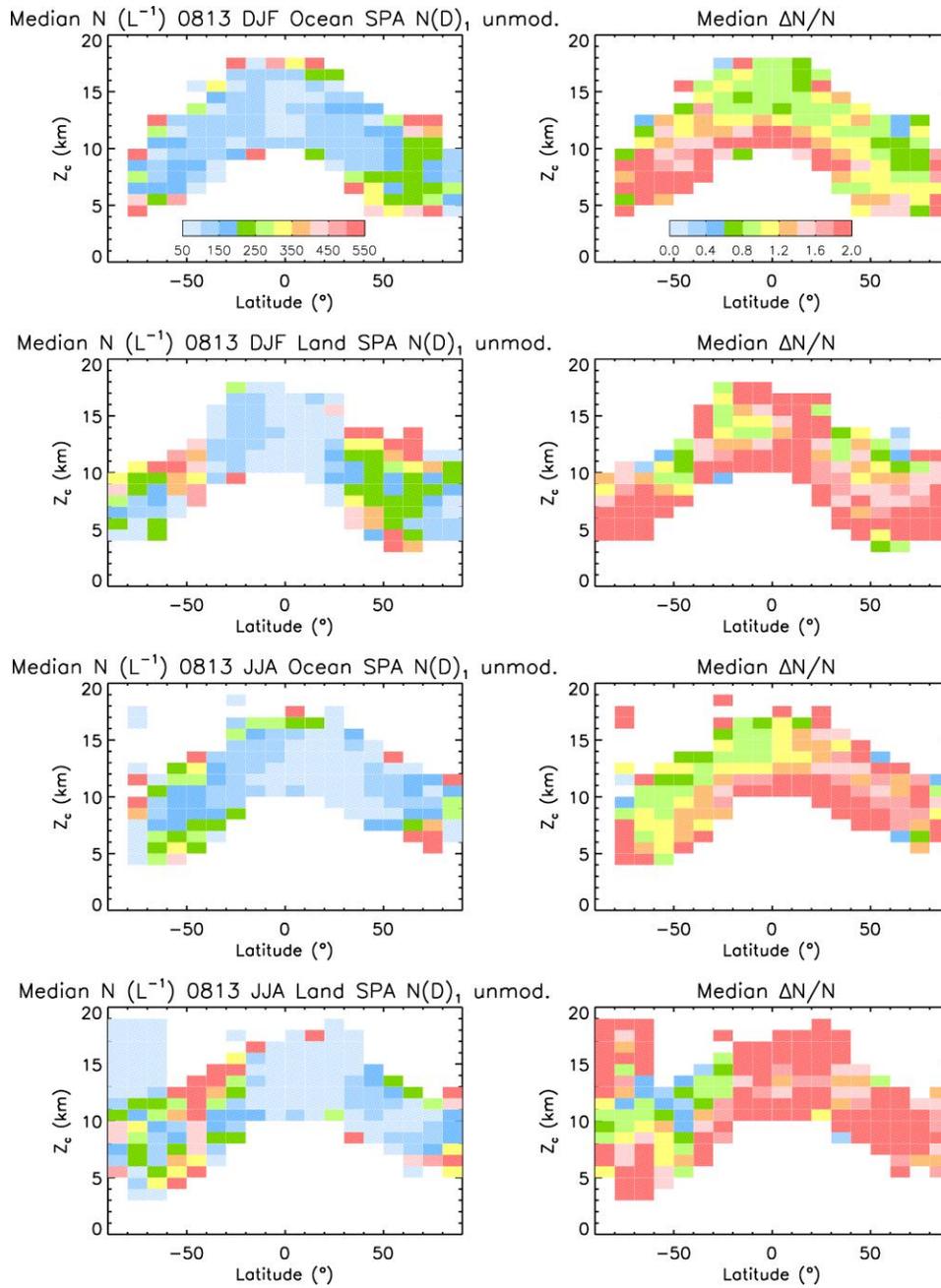
Median N (L⁻¹) 0813 DJF Ocean SPA N(D)₁ unmod.   Median ΔN/N

Median N (L⁻¹) 0813 DJF Land SPA N(D)₁ unmod.   Median ΔN/N

Median N (L⁻¹) 0813 JJA Ocean SPA N(D)₁ unmod.   Median ΔN/N

Median N (L⁻¹) 0813 JJA Land SPA N(D)₁ unmod.   Median ΔN/N

Fig. S10. Same as Fig. 9 in the main paper, but by relaxing the OD threshold to OD > 0.1.

Figure S11. Samples count vs. the representative cloud temperature T_c and T_c - T_{top} at 0-30° (TRO, left), 30-60° (MID, center), and 60-82° (HIGH, right) during 2008 and 2013. Overplotted are isolines of T_{base} - T_{top} (solid: 15 K, dashed: 25 K; dotted: 35 K). Panels from top to bottom are for winter over oceans, winter over land, summer over oceans, and summer over land.
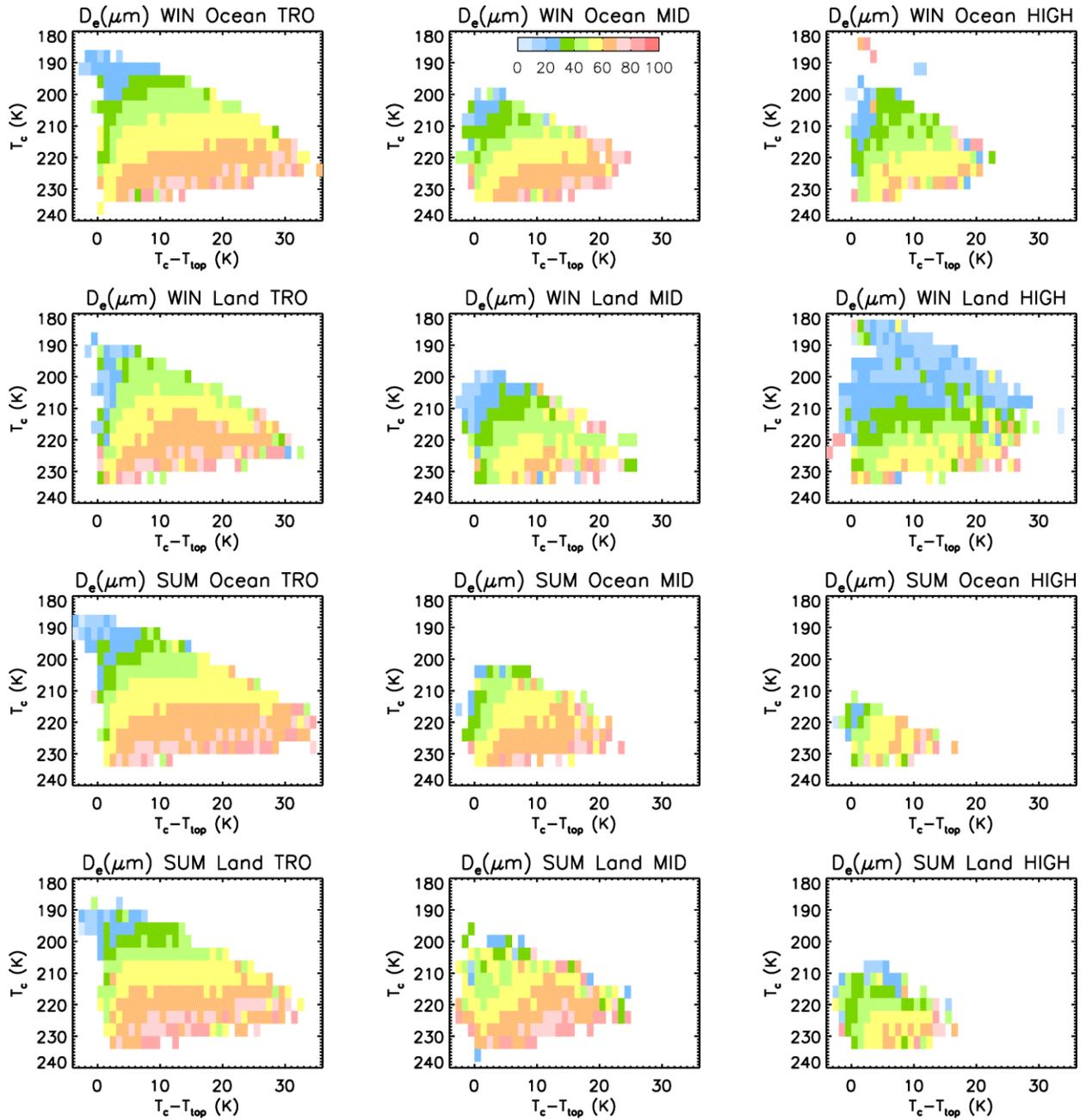
Figure S12: Median retrieved D_e (μm) using the SPARTICUS N(D)$_1$ unmodified formulation vs. the representative cloud temperature T_c and T_c - T_{top} at 0-30° (TRO, left), 30-60° (MID, center), and 60-82° (HIGH, right) during 2008 and 2013. Panels from top to bottom are for winter over oceans, winter over land, summer over oceans, and summer over land.
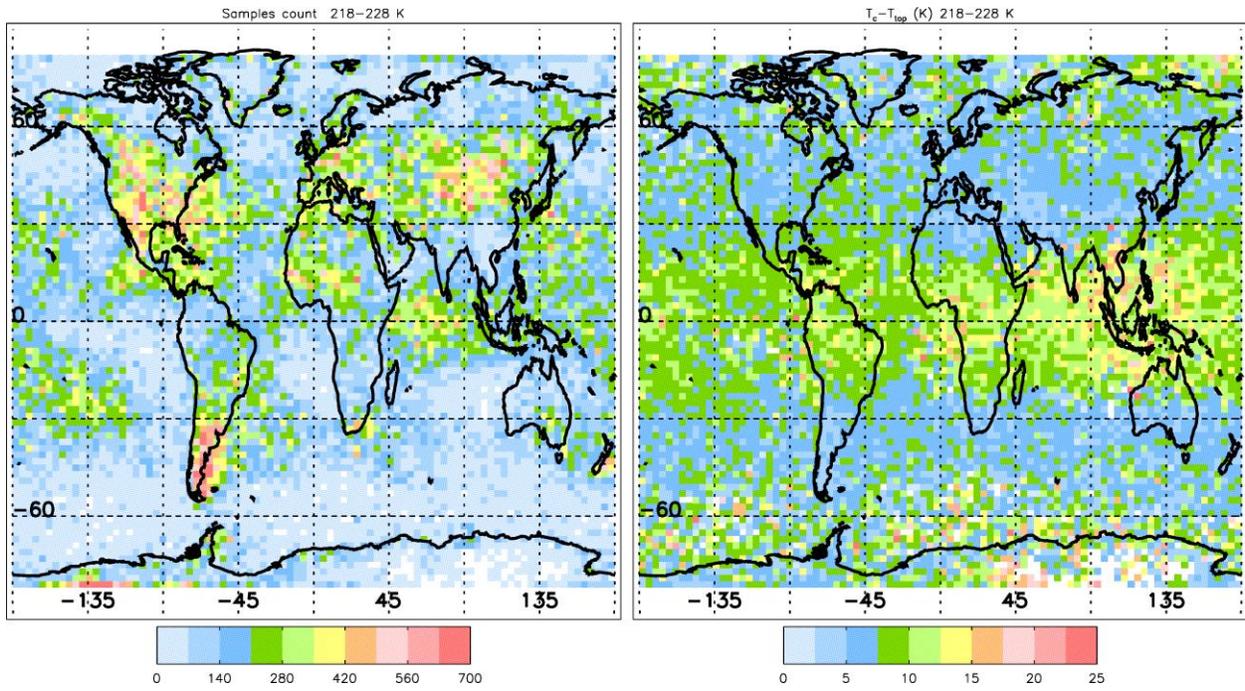
Figure S13: Geographical distribution of (left) number of samples and (right) median $T_c - T_{top}$ values during 2008 and 2013 where the cloud layer representative temperature, T_c, is between 218 and 228 K.